Ceramics International xxx (xxxx) xxx

Contents lists available at ScienceDirect

Ceramics International

journal homepage: www.elsevier.com/locate/ceramint

EPR and optical study of erbium-doped CeO_2 and CeO_2 / CeF_3 nanoparticles

M.S. Pudovkin [a], O.A. Morozov [a,b], S.L. Korableva [a], R.M. Rakhmatullin [a,*], V.V. Semashko [a,b], A.K. Ginkel [a], A.A. Rodionov [a], A.G. Kiiamov [a]

[a] Kazan Federal University, Institute of Physics, 18 Kremlyovskaya Str, Kazan, 420008, Russian Federation
[b] Zavoisky Physical-Technical Institute, FRC Kazan Scientific Center of RAS, Sibirsky Trakt Str. 10, Kazan, 420029, Russian Federation

ARTICLE INFO

Handling Editor: Dr P. Vincenzini

Keywords:
CeO_2
CeF_3
Nanocomposites
EPR

ABSTRACT

Here, the facile dry synthesis of composite CeO_2/CeF_3 nanoparticles doped with Er^{3+} probe ions using ammonium bifluoride (NH_4HF_2) is reported. This method allows synthesizing composite nanoparticles with different ratio of CeO_2 and CeF_3. The structural properties of the composite nanoparticles were studied using XRD, SEM, and TEM techniques, which confirmed the formation of composite CeO_2/CeF_3 nanoparticles. The luminescence spectra show that the intensity of the Ce^{3+} peak increases after fluorination procedure, revealing the fact that the amount of Ce^{3+} is increased. In particular, the total 4f-4f luminescence intensity of CeO_2/CeF_3:Er^{3+}(0.1 at.%) nanoparticles is 3.5 time higher compared to CeO_2:Er^{3+}(0.1 at.%) ones under both UV or resonant pumping. Probably it can be associated with the increased concentration of trivalent rare-earth ions in a cubic-distorted environment. The same tendency is observed for the excitation spectra. EPR measurements showed that fluorination of CeO_2 nanoparticles doped with different concentration of Er^{3+} ions leads to the formation of trigonal sites in ceria nanoparticles.

1. Introduction

Rare earth-based nanoparticles (NPs) are promising nanomaterials for applications in various areas such as catalysis, medicine, optoelectronics, bio-imaging [1,2], and temperature sensing [3]. Among them cerium dioxide and cerium fluoride NPs doped with rare-earth ions are attractive subject for researchers due to the features that include low phonon energy [4,5], which leads to the decrease of non-radiative transition probability increasing the luminescence intensity. This fact makes CeO_2 and CeF_3 excellent host-matrices for optical applications. There are numerous publications devoted to the applications of both types of cerium NPs for catalysis and medical purposes. Cerium dioxide NPs (or ceria - CeO_2) has been extensively studied due to its great properties such as the oxygen storage capacity as well as the ability to keep its fluorite-type structure at a high concentration of oxygen vacancies. These properties related to the easy transition between Ce^{4+} and Ce^{3+} oxidation states in ceria that are accompanied by the formation of oxygen vacancies in the structure [6]. The presence of both Ce^{4+} and Ce^{3+} ions provides redox activity on the surface of CeO_2 NPs and exert outstanding antioxidant effects. It allows CeO_2 NPs acting as anti-inflammatory agents, with them being potentially innovative therapeutic tools [7–9]. CeO_2 NPs can be easily converted to CeF_3 NPs that also can be used for biomedical applications [10]. Recently there was a publication devoted to the experimental evidence of the mitogenic action of cerium dioxide and cerium fluoride NPs via observation of the regeneration of a whole organism – freshwater flatworms Schmidtea mediterranea (planarian) [11]. CeF_3 NPs were shown to protect both organic molecules (organic dyes) and living cells (testicular cells) from the oxidative activity of hydrogen peroxide [12].

In the case of optical applications, rare-earth doped CeO_2 or CeF_3 NPs are highly promising as up-conversion materials in biological labeling, multimodal bioimaging, photodynamic therapy, and drug delivery [10]. Both CeO_2 and CeF_3 are capable of generating reactive oxygen species under external irradiation (UV or X-ray irradiation) in aqueous media, that makes them promising candidates as inorganic photosensitizers for X-ray induced photodynamic therapy as well as for photocatalysis [13, 14]. Moreover, the cerium ion in the inorganic host acts as a sensitizer converting X-ray irradiation in the UV one. This property is also demanded in the X -ray induced photodynamic therapy, where cerium-based NPs convert X –ray in the visible light that activates

* Corresponding author.
E-mail address: rafail.rakhmatullin@kpfu.ru (R.M. Rakhmatullin).

https://doi.org/10.1016/j.ceramint.2023.12.242
Received 7 September 2023; Received in revised form 23 November 2023; Accepted 18 December 2023
Available online 27 December 2023

organic photosensitizers conjugated with the surface of Ce-based NPs [15].

Particularly, CeF_3 NPs co-doped with Yb^{3+} and Tm^{3+} are proposed to be used for photocatalytic nitrogen fixation [16]. In its turn, Zn^{2+}, Tb^{3+}: CeO_2 phosphors can be used as optical temperature sensors operating in the 303–523 K temperature range [17].

Prominent properties of CeO_2 and CeF_3 NPs can be combined by synthesizing composite CeO_2/CeF_3 NPs.

Recently we presented the works devoted to the synthesis of composite CeO_2/CeF_3 NPs using annealing of CeO_2 NPs in tetrafluoromethane (CF_4) and tetrafluoroethane (HFC-134a) gases [18,19]. The characterization of the obtained composite NPs with XRD, TEM, and optics proved the formation of CeF_3 structure on the CeO_2 nanoparticles. In this paper we report on a dry synthesis using ammonium bifluoride NH_4HF_2 and characterization of composite CeO_2/CeF_3 nanoparticles doped with Er^{3+} probe ions. The formation of double-phase CeO_2/CeF_3 NPs can provide the synergy of excellent properties of both CeO_2 and CeF_3. In its turn, the doping procedure can increase the number of applications. For example, it could be used for temperature sensing, X-ray induced photodynamic therapy, catalysis, up and down conversion and other fields.

2. Experimental techniques

The phase composition of the powders was studied by X-ray diffraction method (XRD) using Bruker D8 Advance X-ray diffractometer (Cu Kα radiation λ = 0.154 nm). TEM analysis of the studied samples was carried out in a transmission electron microscope Hitachi HT7700 Exalens with an accelerating voltage of 100 kV.

Scanning Electron Microscopy (SEM) images and EDS spectra were obtained with multipurpose analytical complex Merlin (Carl Zeiss).

Fluorescence spectra were recorded using HORIBA Fluorolog QM-75-22-C spectrofluorometer with attached Hamamatsu R13456-11 photomultiplier. The spectral resolution of the device was 0.25 nm.

The EPR measurements were made using continuous wave spectrometer operating at ~9.4 GHz (X-band, Bruker ESP-300). The modulation frequency was 100 kHz, the modulation amplitude 1 G, the power level varied within of 2.5–25 mW to avoid the saturation. Low temperatures were obtained using a commercial liquid-helium flow cryostat system (Oxford Instruments).

3. Samples preparation and their characterization

CeO_2:Er^{3+} NPs were synthesized using the co-precipitation technique from aqueous solution of $Ce(NO_3)_3$*$6H_2O$ + $Er(NO_3)_3$*$5H_2O$ powders and hexamethylenetetramine $(CH_2)_6N_4$, (HMTA) [20–22]. The precursor of erbium ions was $Er(NO_3)_3$*$5H_2O$ which was taken in the amount to obtain 0.01 at.%, 0.1 at.% of Er^{3+} ions in CeO_2 nanoparticles. Aqueous solutions of $Ce(NO_3)_3$*$6H_2O$ (purity 99.95 %) + $Er(NO_3)_3$*$5H_2O$ (purity 99,95 %) and HMTA (purity 99.9 %) were filtered and then mixed and kept at room temperature for 15 h. Next, the solution was heated to 60 °C and kept at this temperature for an hour during which the mixture was stirred on a magnetic stirrer. Throughout the process the acidity of the solution was kept at pH = 6. After the heating, the solution was cooled down for 24 h.

The precipitated oxides were collected by centrifugation of the mixture at a rate of 9000 rpm for 10 min. The solution was drained, and the particles remaining at the bottom were broken up using an ultrasonic bath for half an hour. The washing process was repeated five times. The resulting nanopowders were dried at 50 °C for 24 h and typically were annealed under air at 600 °C for 4 h in the muffle furnace.

Notations of the prepared samples are given in Table 1. CeO_2 NPs denoted as samples 1 and 3 differ only by concentration of Er^{3+} ions.

Composite CeO_2/CeF_3 NPs (samples 2, 4) were obtained by fluorination of corresponding CeO_2 NPs (samples 1, 3). This has been done by annealing CeO_2 NPs in fluorine atmosphere [23]. In the previous works [18,19] we used tetrafluoromethane (CF_4) and tetrafluoroethane (HFC-134a) gases to get composite CeO_2/CeF_3 NPs. However, in the case of using above mentioned techniques it is difficult to control the ratio between the formed CeO_2 and CeF_3 structures. In this study we applied ammonium hydrogen fluoride (ammonium bifluoride) for the dry synthesis process that was described in reference [24]. The CeO_2 NPs and ammonium bifluoride $(NH_4H)F_2$ were thoroughly mixed and placed in the muffle furnace. It is known that the ammonium bifluoride decomposes in the range of 120–220 °C, and the melting point according to papers [25,26] is 126.5 °C. Thus, CeO_2 NPs interact with molten ammonium bifluoride at a temperature above the melting point.

Table 1
Notations and composition of studied samples.

Sample notation	Composition	annealing temperature	Fluorination temperature
1	CeO_2 : 0.01 at.%Er^{3+}	600 °C air, 4 h	–
2	25%CeO_2/75%CeF_3 : 0.01 at.%Er^{3+}	600 °C air, 4 h	300 °C, 2 h
3	CeO_2 : 0.1 at.%Er^{3+}	600 °C air	–
4	50%CeO_2/50%CeF_3 : 0.1 at.%Er^{3+}	600 °C air, 4 h	300 °C, 2 h
5	CeF_3 : 0.1 at.%Er^{3+}	–	–

The chemical reaction can be described as following [27,28].

$$2\ CeO_2 + 8\ NH_4HF_2 = 2\ CeF_3 + 8\ NH_4F + 4H_2O + F_2$$

This reaction took place at 300 °C in glassy carbon crucibles for 2 h. Using this method, we could choose the ratio between CeO_2 and ammonium bifluoride to get structure with different weights of CeO_2 and CeF_3, for example we could get 50 %, 75 % or 100 % of CeF_3 from whole amount of fluorinated CeO_2. Hereinafter we denote fluorinated CeO_2 nanoparticles as CeO_2/CeF_3 NPs.

The reference sample 5 (CeF_3: 0.1 at.%Er^{3+}) NPs for EPR measurements was prepared using the precipitation technique by mixing stoichiometric solution of cerium nitrate $Ce(NO_3)_3$*$6H_2O$ (purity 99.95 %), $Er(NO_3)_3$*$5H_2O$ (purity 99,95 %) and ammonium fluoride NH_4F (purity 99.99 %). The mixture was kept for 20 min with continuous stirring of the solution, then centrifuged and washed with distilled water, and this process was repeated three times. The resulting product was dried at 50 °C for 24 h.

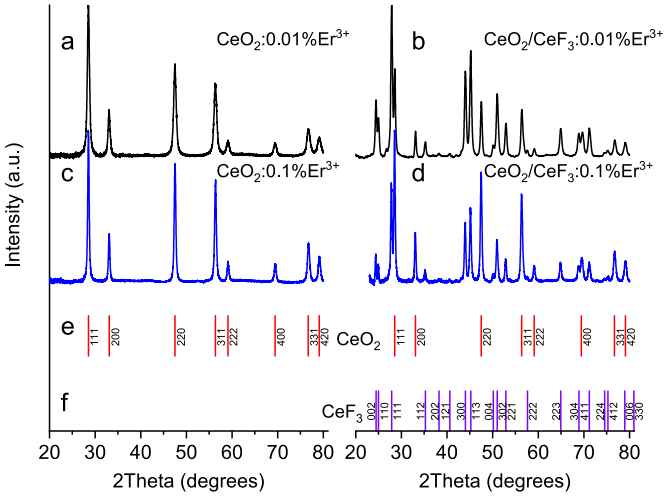

Fig. 1. XRD patterns of CeO_2 NPs doped with Er^{3+} ions before and after fluorination
a) CeO_2: 0.01 at.%Er^{3+} NPs air annealed. **b)** XRD pattern of 25%CeO_2/75% CeF_3: 0.01 at.%Er^{3+} NPs. **c)** XRD pattern of CeO_2: 0.1 at.%Er^{3+} NPs air annealed. **d)** XRD pattern of 50%CeO_2/50%CeF_3: 0.1 at.%Er^{3+} NPs. **e)** Peaks positions for CeO_2 **f)** Peaks positions for CeF_3.

XRD spectra of the NPs samples are shown in Fig. 1. Analysis of obtained spectra shows that after fluorination of ceria NPs with the applied method the structure of CeF_3 is formed. The simulations and calculations of XRD peaks were carried out using the Vesta program [29].

The size of the NPs was estimated from the TEM images using the freeware ImageJ program. Statistics are based on the analysis of 120–160 nanoparticles. The TEM images and size distribution histograms of CeO_2 NPs doped with Er^{3+} ions are shown in Fig. 2. Histogram plots were obtained with the OriginPro 8.1 software. To get the diameter (D) of the NPs, the area (in squire nanometers) of each nanoparticle from TEM image was equated to the area of a circle $\pi \cdot D^2/4$, where $\pi = 3.14$, D is the diameter.

The CeO_2 particle sizes determined by TEM agree well with the X-ray powder diffraction data.

EDS spectra at 30 different spots of SEM images of the studied samples were measured and as example of the SEM (a) image along with the EDS spectrum (b) are presented in Fig. 3. It was found that in some of the spots the fluorine atom is detected whereas in some other spots it is absent. We suppose that some small part of CeO_2 NPs was not fluorinated most probably due to insufficient mixing of ammonium bifluoride and CeO_2 NPs. This fact has led us to conclusion that obtained fluorinated nanoparticles are not core shell but mixture of core-shell and partially fluorinated CeO_2/CeF_3 NPs. However, in average according to XRD patterns obtained NPs have combined structure of CeO_2 and CeF_3 in ratio corresponding applied precursors. The applied synthesis technique is very simple and efficient to control the ratio between CeF_3 and CeO_2 components, but still needs to be improved.

4. Results and discussion

4.1. Optical spectroscopy

Generally, the optical properties of Er^{3+} ions doped in CeO_2 NPs are stipulated by optical transitions of Ce^{3+} and Er^{3+} ions. The 4f-4f luminescence spectra of Er^{3+} ions in CeO_2 NPs were previously studied in Ref. [30]. However, as it was mentioned above, cerium has two oxidation states, 3+ and 4+, and the relative concentration of Ce^{3+} and Ce^{4+} depends on the redox conditions of the sample preparation process. For instance, the fluorination procedure implements the formation of double-phase CeO_2/CeF_3 structure with the increased amount of Ce^{3+}.

The energy level diagram of Ce^{3+}/Er^{3+} system is represented in Fig. 4.

Under Ce^{3+} excitation at 266 nm, the broad Ce^{3+} emission peak centered at ~440 nm is clearly observed. There is also energy transfer from Ce^{3+} to Er^{3+} via $^4F_{5/2}$ excited sate of Er^{3+}. Also there are non-radiative transitions from excited $^4F_{5/2}$ state to lower $^2H_{11/2}$ and $^4F_{9/2}$ ones.

The optical spectra of Ce^{3+} ions in UV and visible spectral ranges are determined by the allowed electric dipole 4f↔5d interconfigurational transitions. In contrast, the Ce^{4+} ion does not have 4f electrons and therefore does not have optical spectra. The increase of Ce^{3+} amount must increase the absorption of UV radiation and vice versa. This is confirmed by excitation and luminescence spectra.

The excitation spectrum of Er^{3+}-fluorescence demonstrates (Fig. 5) a broad peak in the ~300–400 nm range corresponding to the absorption band due to 4f-5d transitions of Ce^{3+} in CeO_2. Also, there are narrow peaks in the visible spectrum which correspond to the transitions from $^4I_{15/2}$ ground state to the excited $^4F_{5/2}$, $^4F_{7/2}$ и $^2H_{11/2}$ manifolds of Er^{3+} ions. According to the excitation spectra, the intensity of Ce^{3+} peak increases after the fluorination procedure revealing the fact, that the amount of Ce^{3+} is increased. The same tendency is observed for the luminescence spectra.

Room-temperature luminescence spectra of air annealed CeO_2: 0.1% Er^{3+} NPs and fluorinated NPs under excitation into 4f-5d band of Ce^{3+} ions or into the CeO_2 charge-transfer (CT) band [31] at 355 nm and under resonant excitation to $^4I_{15/2} \rightarrow {}^2H_{11/2}$ transitions of Er^{3+} ions at 517 nm are presented in Fig. 6, a) and b), correspondently. Both luminescence spectra consist of intensive line groups due to $^2H_{11/2}$-$^4I_{15/2}$ (λ = 509–534 nm), $^4S_{3/2}$-$^4I_{15/2}$ (λ = 535–573 nm) and $^4F_{9/2}$-$^4I_{15/2}$ (λ = 635–703 nm) 4f-4f transitions of Er^{3+} ions. Moreover, the intensive 5d-4f luminescence of Ce^{3+} ions in CeO_2/CeF_3:Er^{3+}(0.1 at.%) NPs is detected under the UV excitation. In particular, the total intensity of 4f-4f luminescence of CeO_2/CeF_3:Er^{3+}(0.1 at.%) NPs is 3.5 time higher

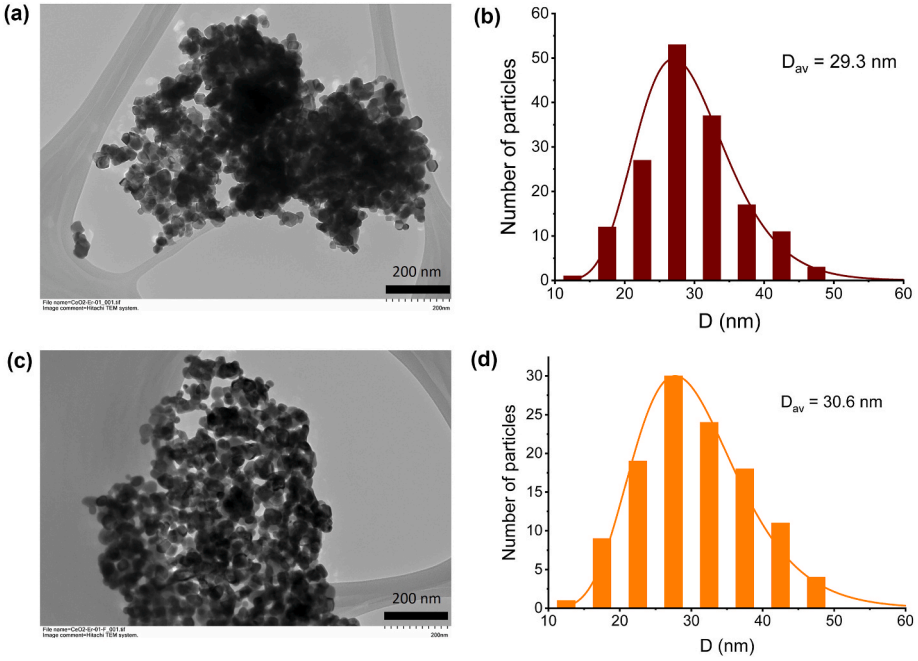

Fig. 2. The TEM images and size distribution histograms of CeO_2 NPs doped with Er^{3+} ions. **a)** TEM image of CeO_2: 0.1 at.%Er^{3+} NPs air annealed. **b)** The size distribution histogram of CeO_2: 0.1 at.%Er^{3+} NPs air annealed. **c)** TEM image of CeO_2/CeF_3: 0.1 at.%Er^{3+} NPs. **d)** The size distribution histogram of CeO_2/CeF_3: 0.1 at.%Er^{3+} NPs.

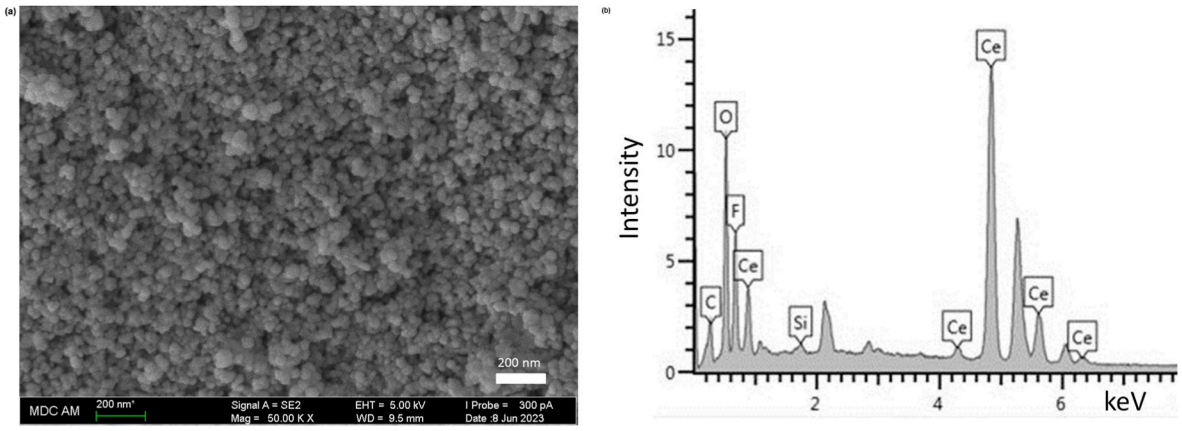

Fig. 3. SEM image (**a**) and EDS spectrum (**b**) at some spot of CeO_2/CeF_3: 0.1 at.% Er^{3+} NPs.

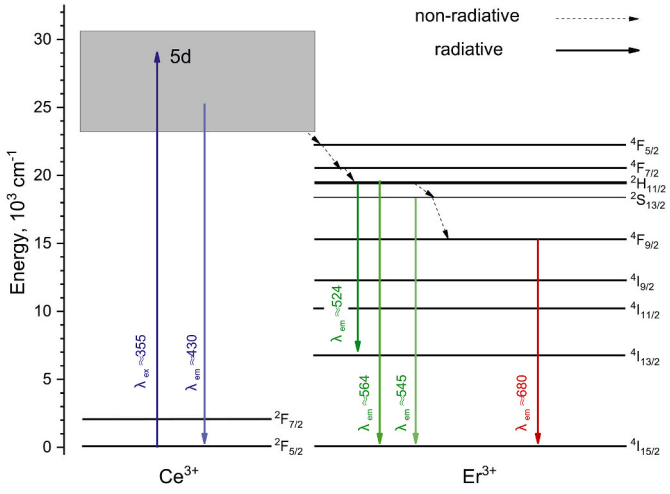

Fig. 4. The energy level diagram of Ce^{3+}/Er^{3+} system.

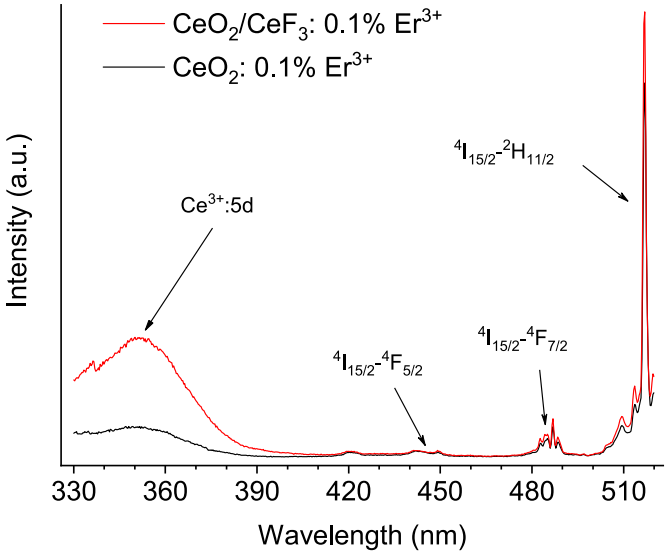

Fig. 5. The room temperature excitation spectrum of CeO_2: 0.1%Er^{3+} and CeO_2/CeF_3: 0.1 at.% Er^{3+} (λ_{em} = 545,5 nm, Er^{3+}, $^4S_{3/2}$ – $^4I_{15/2}$ transition).

compared to CeO_2:Er^{3+}(0.1 at.%) one under both UV or resonant excitations. Probably it can be associated with the increased concentration of trivalent rare-earth ions in a cubic-distorted environment and the observed phenomena require further studies. The normalized at 546 nm Er^{3+} peak room temperature luminescence spectra of Er^{3+}-doped CeO_2 and CeO_2/CeF_3 sample are presented at Fig. S1 of supplementary file. It can be seen, that the shape of the Er^{3+} spectra is not significantly affected by the formation of double-phase sample. It can be explained by the shielded nature of the 4f shell of Er^{3+}. Hence, the probabilities of radiative transitions are almost constant. On the other hand, after annealing there is an interplay between intensities of Stark peaks of Er^{3+} emission ($^4S_{3/2}$ – $^4I_{15/2}$ radiative transition). This interplay can be related to the formation of the second phase after annealing and changes in crystal field.

4.2. EPR spectroscopy

The first observation of EPR lines of Er^{3+} ions due to cubic sites in ceria NPs was reported in the publication [30]. The spectra in Ref. [30] were similar to EPR of Er^{3+} ($4f^{11}$, $^4I_{15/2}$) ions in CeO_2 crystals that were first studied in the works [32,33]. The features of EPR spectroscopy of rare earth ions in solids are described in detail in the fundamental monograph by A.Abragam and B.Bleaney [34]. Y. Komet et al. [32] reported about observation of the isotropic line due to the cubic site with $g = 6.759 \pm 0.005$ and measured a hyperfine constant $A_{7/2}(Er^{167}) = 72.7 \pm 0.3$ G, M.M. Abraham et al. [33] reported close g-value for the cubic site with $g = 6.747 \pm 0.006$ and the hyperfine constant of 73.7 ± 0.1 G but also found two sets of axial sites with $g_{||} = 10.25 \pm 0.05$, $g_{\perp} = 4.847 \pm 0.005$ (the first set), $g_{||} = 4.539 \pm 0.005$, $g_{\perp} = 7.399 \pm 0.007$ (the second set). In the previous study [30] no axial EPR lines were detected in ceria NPs. It should be noted that in the publication [30] the concentration of Er^{3+} ions was rather small, ~0.002 at.% and ~0.005 at.% in the studied samples which may explain the difficulty in detecting axial lines in a powder at such concentrations. In this work we present EPR results for higher concentration of Er^{3+} ions in CeO_2 and CeO_2/CeF_3 NPs that are shown in Fig. 7. Fig. 7a shows EPR spectra detected in the CeO_2 (sample 1) and CeO_2/CeF_3 NPs (sample 2) containing 0.01 at.% of Er^{3+} ions. Both spectra consist of intensive line from even isotopes of Er^{3+} ions with g ~6.76 assigned to cubic sites and less intensive hyperfine lines due to odd isotope (I = 7/2) of Er^{167} (22.94 % abundance). Besides the EPR lines due to cubic sites the EPR spectrum of CeO_2/CeF_3 NPs has an additional line with g ~4.84. We assigned this line to the trigonal site that is close to the axial site with $g_{\perp} = 4.847$ observed by M. M. Abraham et al. [33]. The trigonal sites of Er^{3+} ions in CeO_2 crystals were also observed by A.A. Antipin et al. [35] who gives g-values of $g_{||} = 10.3 \pm 0.05$, $g_{\perp} = 4.84 \pm 0.02$. To prove that we detected the trigonal line in CeO_2 we made the simulation of the EPR spectrum using the

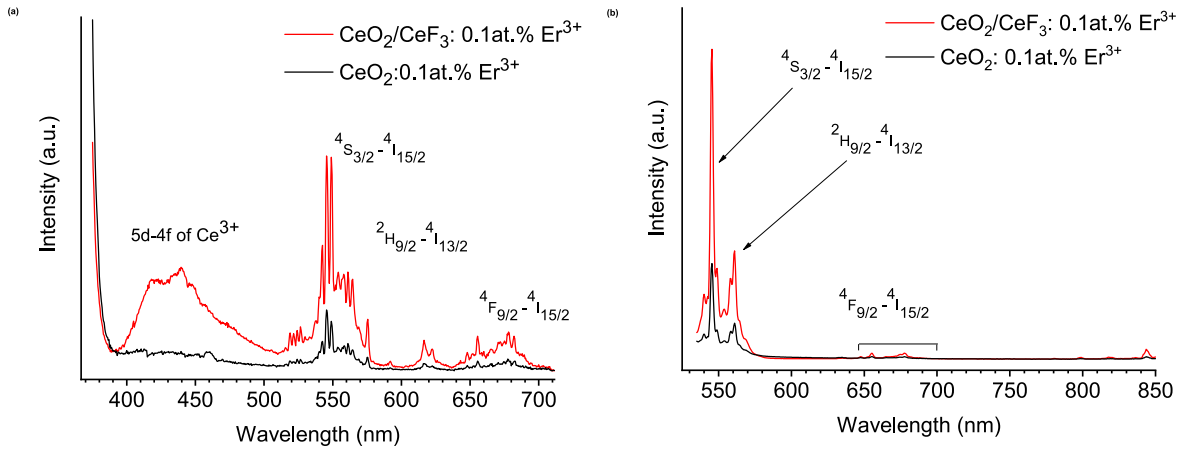

Fig. 6. Room-temperature luminescence spectra of CeO_2: 0.1%Er^{3+} and CeO_2/CeF_3: 0.1 at.% Er^{3+} NPs under excitation at λ_{ex} = 355 nm (**a**) and λ_{ex} = 517 nm (**b**).

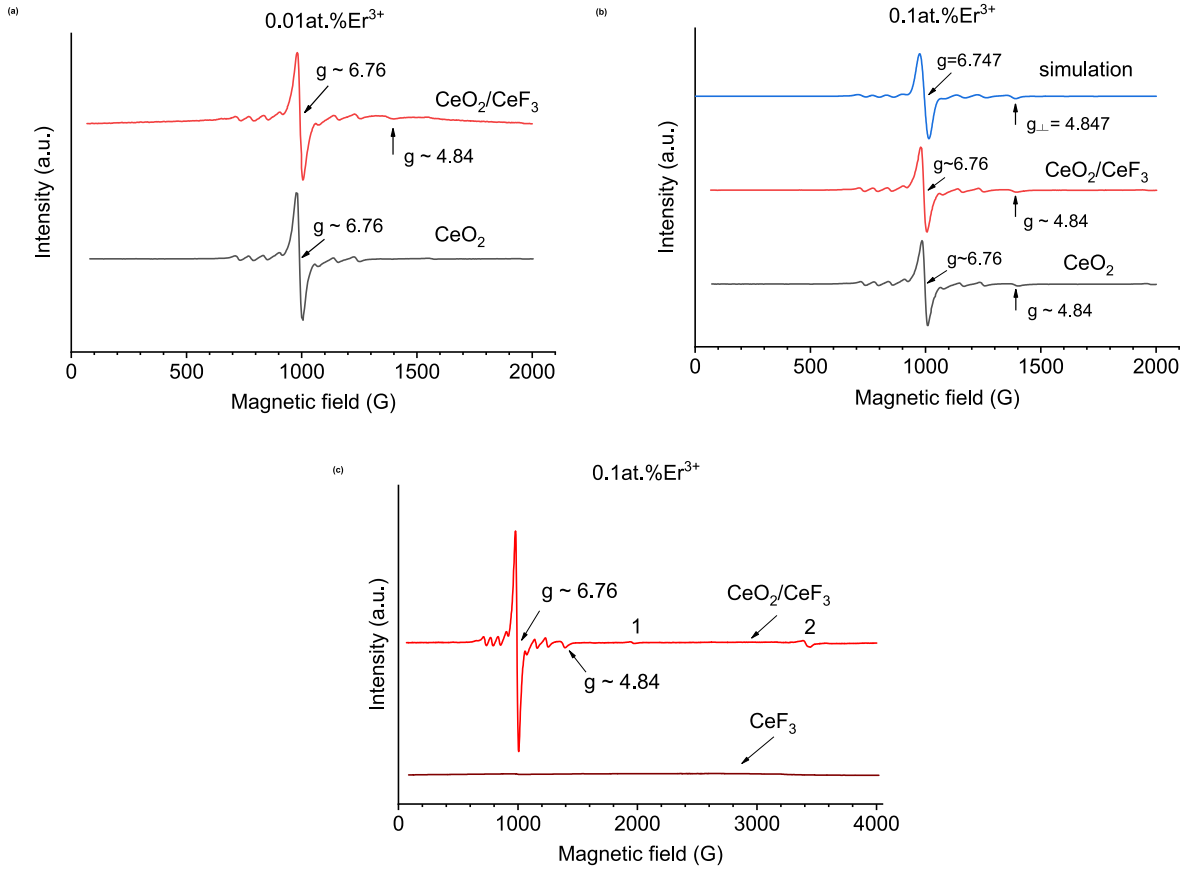

Fig. 7. EPR spectra of Er–doped CeO_2 and CeO_2/CeF_3 NPs at 15K, X-band. **a**) EPR spectra of 25%CeO_2/75%CeF_3: 0.01 at.%Er^{3+} NPs and CeO_2: 0.01 at.%Er^{3+} NPs. **b)** Simulated EPR spectrum and EPR spectra of 50%CeO_2/50%CeF_3: 0.1 at.%Er^{3+} NPs and of CeO_2: 0.1 % Er^{3+} NPs. **c)** Extended EPR spectra of 50%CeO_2/50%CeF_3: 0.1 at.%Er^{3+} NPs and CeF_3:0.1 % Er^{3+} NPs.

EasySpin software package [36] and $g_{||}$, $g_{\perp}$ (the first set), A –values were taken from the paper by M.M. Abraham et al. [33]. The result of simulation is shown in Fig. 7b along with experimental spectra for CeO_2: 0.1 % Er^{3+} (sample 3) and CeO_2/CeF_3:0.1 % Er^{3+} (sample 4) NPs. Simulations revealed that the ratio of weights of cubic sites to trigonal sites is 5. We can conclude that 20 % of Er^{3+} ions occupy trigonal symmetry sites. The last sites are formed due to defects along <111> axis of crystalline structure that can be oxygen vacancies. Thus, it is possible to estimate the number of defects using the ratio of cubic and axial symmetry sites.

As can be seen on Fig. 7b there is no notable differences in EPR spectra of Er^{3+} ions between air annealed and fluorinated CeO_2: 0.1 % Er^{3+} samples, in both spectra there is the trigonal line. This differs from EPR spectra for lower concentration of Er^{3+} ions shown in Fig. 7a. We explain this by following. The higher concentration of Er^{3+} ions in CeO_2 lattice the more probability to form defects like oxygen vacancies along <111> axis that lead to local trigonal symmetry and corresponding EPR line. In case of lower concentration, the trigonal symmetry can be caused by fluorination, when an oxygen ion is substituted by fluorine ion. As noted above, XRD measurements show that fluorination of CeO_2 NPs leads to the formation of CeF_3 structure on the part of these

nanoparticles. Because CeO_2 and CeF_3 have different structures, cubic and hexagonal ones, it could be expected that EPR spectra of Er^{3+} ions reveal new lines. However, CeF_3 is a paramagnetic and magnetic interaction between host Ce^{3+} ions and doped Er^{3+} ions should lead to the broadening of resonance lines. Such broadening up to 500 G for the line corresponding to the central transition (−1/2<−> 1/2) was observed at helium temperature for Gd^{3+} ions (0.01 mol.%) in CeF_3 bulk crystals by S.K. Misra et al. [37]. Note that the broadening can be much larger for the Er^{3+} ion as compare with Gd^{3+} ion which is the S-state ion. This can explain the absence of additional absorption lines in fluorinated CeO_2 NPs. To prove this, we made EPR measurements of the sample 5 of CeF_3 doped with 0.1 % Er^{3+} and compared the obtained spectrum with the spectrum of fluorinated CeO_2: 0.1 % Er^{3+} (sample 4). The EPR measurements of both samples were made at the same conditions and parameters and corresponding spectra are shown in Fig. 7c. Thus, the main contribution to the EPR spectrum of composite CeO_2/CeF_3:0.1 % Er^{3+} NPs produce the CeO_2:0.1 % Er^{3+} part of NPs. Fluorination of CeO_2 NPs can lead to additional defects like trigonal EPR line. Fig. 7c shows extended EPR spectrum of CeO_2/CeF_3:0.1 % Er^{3+} NPs that include also weak lines 1 and 2. The weak EPR line 1 with g ~3.42 we assigned to the trace impurity of Yb^{3+} ions in the cubic site of CeO_2 [32]. The other line 2 with g~1.96 most probably due to the small amount of Gd^{3+} ions [38].

Thus, we can conclude from EPR measurements that fluorination lead to formation of axial sites in ceria NPs.

5. Conclusions

In this work we present a new facile dry synthesis of composite CeO_2/CeF_3 NPs doped with rare earth ions and this technique allows varying the ratio between CeO_2 and CeF_3 components.

XRD measurements prove the formation of CeF_3 structure with the applied technique.

The size of CeO_2/CeF_3 NPs was estimated via the TEM technique that corresponds to data obtained from linewidth XRD measurements using Scherrer equation.

EPR measurements show that fluorination of CeO_2 NPs leads to the formation of axial sites in CeO_2 fluorite structure.

Fluorination of CeO_2 NPs to produce composite NPs of Er-doped CeO_2/CeF_3 in different proportion allows one to combine properties of cerium oxide and cerium fluoride NPs.

Data availability

The data from this research are available on request from the authors.

Declaration of competing interest

The authors declare that they have no known competing financial interests or personal relationships that could have appeared to influence the work reported in this paper.

Acknowledgements

The authors gratefully acknowledge the CSF-SAC FRC KSC RAS for providing necessary facilities to carry out this work.

The synthesis, optical, and EPR experiments were funded by the subsidy allocated to Kazan Federal University for the state assignment in the sphere of scientific activities (project number FZSM-2023-0012). The XRD experiments were funded by the Kazan Federal University Strategic Academic Leadership Program (PRIORITY-2030).

Authors are grateful to V.I. Kolesnikova for the help with TEM images processing and to A.G. Shmelev for the help with optical measurements.

Appendix A. Supplementary data

Supplementary data to this article can be found online at https://doi.org/10.1016/j.ceramint.2023.12.242.

References

[1] C. Chen, C. Li, Z. Shi, Current advances in lanthanide-doped upconversion nanostructures for detection and bioapplication, Adv. Sci. 3 (2016), 160029, https://doi.org/10.1002/advs.201600029.

[2] C. Walkey, S. Das, S. Seal, J. Erlichman, K. Heckman, L. Ghibelli, E. Traversa, J. F. McGinnis, W.T. Self, Catalytic properties and biomedical applications of cerium oxide nanoparticles, Environ. Sci.: Nano 2 (2015) 33–53, https://doi.org/10.1039/C4EN00138A.

[3] A.D. Pickel, A. Teitelboim, E.M. Chan, N.J. Borys, P.J. Schuck, C. Dames, Apparent self-heating of individual upconverting nanoparticle thermometers, Nat. Commun. 9 (2018) 4907, https://doi.org/10.1038/s41467-018-07361-0.

[4] M.J. Weber, Probabilities for radiative and nonradiative decay of Er^{3+} in LaF_3, Phys. Rev. 157 (1967) 262–272, https://doi.org/10.1103/PhysRev.157.262.

[5] J.W. Stouwdam, F.C.J.M. van Veggel, Near-infrared emission of redispersible Er^{3+}, Nd^{3+}, and Ho^{3+} doped LaF_3 nanoparticles, Nano Lett. 2 (2002) 733–737, https://doi.org/10.1021/nl025562q.

[6] M. Mogensen, N.M. Sammes, G.A. Tompsett, Physical, chemical and electrochemical properties of pure and doped ceria, Solid State Ionics 129 (2000) 63–94, https://doi.org/10.1016/S0167-2738(99)00318-5.

[7] L. Rubio, R. Marcos, A. Hernández, Nanoceria acts as antioxidant in tumoral and transformed cells, Chem. Biol. Interact. 291 (2018) 7–15, https://doi.org/10.1016/j.cbi.2018.06.002.

[8] N. Thakur, P. Manna, J. Das, Synthesis and biomedical applications of nanoceria, a redox active nanoparticle, J. Nanobiotechnol. 17 (2019) 84, https://doi.org/10.1186/s12951-019-0516-9.

[9] E. Casals, M. Zeng, M. Parra-Robert, G. Fernández-Varo, M. Morales-Ruiz, W. Jimenez, V. Puntes, G. Casals, Cerium oxide nanoparticles: advances in biodistribution, toxicity, and preclinical exploration, Small 16 (2020), 1907322. https://onlinelibrary.wiley.com/doi/10.1002/smll.201907322.

[10] C. Li, J. Lin, Rare earth fluoride nano-/microcrystals: synthesis, surface modification and application, J. Mater. Chem. 20 (2010) 6831–6847, https://doi.org/10.1039/c0jm00031k.

[11] A. Ermakov, A. Popov, O. Ermakova, O. Ivanova, A. Baranchikov, K. Kamenskikh, T. Shekunova, A. Shcherbakov, N. Popova, V. Ivanov, The first inorganic mitogens: cerium oxide and cerium fluoride nanoparticles stimulate planarian regeneration via neoblastic activation, Mater. Sci. Eng. C 104 (2019), 109924, https://doi.org/10.1016/j.msec.2019.109924.

[12] A.B. Shcherbakov, N.M. Zholobak, A.E. Baranchikov, A.V. Ryabova, V.K. Ivanov, Cerium fluoride nanoparticles protect cells against oxidative stress, Mater. Sci. Eng. C 50 (2015) 151–159, https://doi.org/10.1016/j.msec.2015.01.094.

[13] S. Clement, W. Deng, E. Camilleri, B.C. Wilson, E.M. Goldys, X-ray induced singlet oxygen generation by nanoparticle photosensitizer conjugates for photodynamic therapy: determination of singlet oxygen quantum yield, Sci. Rep. 6 (2016), 19954. https://www.nature.com/articles/srep19954.

[14] E. Kusmierek, A CeO_2 semiconductor as a photocatalytic and photoelectrocatalytic material for the remediation of pollutants in industrial wastewater: a review, Catalysts 10 (2020) 1435, https://doi.org/10.3390/catal10121435.

[15] A. Nizamutdinov, E. Lukinova, N. Shamsutdinov, P. Zelenikhin, A. Khusainova, M. Gafurov, S. Zinchenko, D. Safin, M. Pudovkin, CeF_3-YF_3-TbF_3 nanoparticle-polymer–"radachlorin" conjugates for combined photodynamic therapy: synthesis, characterization, and biological activity, J. Compos. Sci. 7 (6) (2023) 255, https://doi.org/10.3390/jcs7060255.

[16] M. Zhong, Z. Wang, D. Dai, B. Yang, S. Zuo, C. Yao, F. Wu, X. Li, Upconversion hollow nanospheres CeF_3 co-doped with Yb^{3+} and Tm^{3+} for photocatalytic nitrogen fixation, J. Rare Earths 40 (2022) 586–594, https://doi.org/10.1016/j.jre.2021.03.004.

[17] K.K. Gupta, T.H. Weng, S. Som, C.H. Lu, Synthesis and photoluminescence characterizations of Zn^{2+} and Tb^{3+} codoped CeO_2 phosphors for temperature sensing applications, Ceram. Int. (2023), https://doi.org/10.1016/j.ceramint.2023.07.244.

[18] V.V. Pavlov, R.M. Rakhmatullin, O.A. Morozov, S.L. Korableva, A.G. Kiiamov, A. K. Naumov, V.V. Semashko, V.G. Evtugyn, YuN. Osin, CeO_2/CeF_3 composite nanoparticles: fabrication by fluorination of CeO_2 with tetrafluoromethane gas, Mater. Chem. Phys. 207 (2018) 542–546, https://doi.org/10.1016/j.matchemphys.2017.12.086.

[19] O.A. Morozov, S.L. Korableva, R.M. Rakhmatullin, A.R. Khadiev, A.G. Kiiamov, M. A. Cherosov, M.S. Pudovkin, M.R. Gafurov, Synthesis of core-shell CeO_2/CeF_3 nanoparticles using tetrafluoroethane R-134a, Coatings 12 (2022) 1879, https://doi.org/10.3390/coatings12121879.

[20] P.L. Chen, I.W. Chen, Reactive cerium (IV) oxide powders by the homogeneous precipitation method, J. Am. Ceram. Soc. 76 (1993) 1577–1583, https://doi.org/10.1111/j.1151-2916.1993.tb03942.x.

[21] F. Zhang, Q. Jin, S.-W. Chan, Ceria nanoparticles: size, size distribution, and shape, J. Appl. Phys. 95 (2004) 4319–4326, https://doi.org/10.1063/1.1667251.

[22] O.S. Polezhaeva, N.V. Yaroshinskaya, V.K. Ivanov, Formation mechanism of nanocrystalline ceria in aqueous solutions of cerium(III) nitrate and hexamethylenetetramine, Inorg. Mater. 44 (2008) 51–57, https://doi.org/10.1134/S0020168508010081.

[23] M. Takashima, S. Fukami, Y. Nosaka, T. Unishi, Reaction between rare earth oxides and elemental fluorine. ii. kinetics of the fluorination of cerium dioxide, J. Fluor. Chem. 57 (1992) 131–138, https://doi.org/10.1016/S0022-1139(00)82824-9.

[24] F.H. Spedding, A.H. Daane, The preparation and properties of rare-earth metals, Prog. Nucl. Energy 1 (1956) 413.

[25] J.E. House Jr., Carol S. Rippon, A TG study of the decomposition of ammonium fluoride and ammonium bifluoride, Thermochim. Acta 47 (1981) 213–216, https://doi.org/10.1016/0040-6031(81)85108-8.

[26] E.G. Rakov, E.I. Mel'nichenko, The properties and reactions of ammonium fluorides, Russ. Chem. Rev. 53 (9) (1984) 851–869, https://doi.org/10.1070/RC1984v053n09ABEH003126.

[27] S.J. Patwe, B.N. Wani, U.R.K. Rao, K.S. Venkateswarlu, Synthesis and thermal study of tris(ammonium) hexafluoro metallates(III) of some rare earths, Can. J. Chem. 67 (1989) 1815–1818, https://doi.org/10.1139/v89-281.

[28] M.J. O'Hara, C.M. Kellogg, C.M. Parker, S.S. Morrison, J.F. Corbey, J.W. Grate, Decomposition of diverse solid inorganic matrices with molten ammonium bifluoride salt for constituent elemental analysis, Chem. Geol. 466 (2017) 341–351, https://doi.org/10.1016/j.chemgeo.2017.06.023.

[29] K. Momma, F. Izumi, VESTA 3 for three-dimensional visualization of crystal, volumetric and morphology data, J. Appl. Crystallogr. 44 (2011) 1272–1276, https://doi.org/10.1107/S0021889811038970.

[30] R.M. Rakhmatullin, I.N. Kurkin, V.V. Pavlov, V.V. Semashko, EPR, optical, and dielectric spectroscopy of Er-doped cerium dioxide nanoparticles, Phys. Status Solidi B 251 (2014) 1545, https://doi.org/10.1002/pssb.201451116.

[31] Y. Yang, Y. Cong, D.P. Dong, Y. Xiao, J.Y. Shang, Y. Tong, H.M. Zhang, M. He, J. H. Zhang, Structural and excitation dependent emission properties of octahedral CeO_2:Er^{3+} nanocrystal, J. Lumin. 213 (2019) 427–432, https://doi.org/10.1016/j.jlumin.2019.05.009.

[32] Y. Komet, W. Low, R.C. Linares, Paramagnetic resonance of rare earth ions in cerium oxide, Phys. Lett. 19 (1965) 473–474, https://doi.org/10.1016/0031-9163(65)90108-3.

[33] M.M. Abraham, R.A. Weeks, G.W. Clark, C.B. Finch, Electron spin resonance of rare-earth ions in CeO_2: Yb^{3+} and Er^{3+}, Phys. Rev. 148 (1966) 350–352, https://doi.org/10.1103/PhysRev.148.350.

[34] A. Abragam, B. Bleaney, Electron Paramagnetic Resonance of Transition Ions, Clarendon Press, Oxford, 1970.

[35] A.A. Antipin, Z.N. Zonn, V.A. Ioffe, A.N. Katyshev, L.Y. Shekun, Trivalent rare earths in single crystals of cerium dioxide, Erbium and Ytterbium, Sov. Physics Solid State 9 (1967) 521–522.

[36] S. Stoll, A. Schweiger, J. Magn. Reson. 178 (2006) 42, https://doi.org/10.1016/j.jmr.2005.08.013.

[37] S.K. Misra, G. Bacquet, F. Fabre, EPR of Gd3+ -doped CeF3 single crystal: linewidth variation with temperature, Solid State Commun. 62 (1987) 729–733, https://doi.org/10.1016/0038-1098(87)90035-4.

[38] R.M. Rakhmatullin, L.K. Aminov, I.N. Kurkin, R. Böttcher, A. Pöppl, H. Avila-Paredes, S. Kim, S. Sen, Electron paramagnetic resonance linewidth narrowing of Gd^{3+} ions in Y-doped ceria nanocrystals with decreasing crystallite size, J. Chem. Phys. 131 (2009), 124515, https://doi.org/10.1063/1.3225487.